remote sensing

MDPI

Technical Note

Region-Based Sea Ice Mapping Using Compact Polarimetric Synthetic Aperture Radar Imagery with Learned Features and Contextual Information

Saeid Taleghanidoozdoozan *, Linlin Xu and David A. Clausi

Department of Systems Design Engineering, University of Waterloo, Waterloo, ON N2L 3G1, Canada; l44xu@uwaterloo.ca (L.X.); dclausi@uwaterloo.ca (D.A.C.)
* Correspondence: stalegha@uwaterloo.ca

Abstract: Operational sea ice maps are usually generated manually using dual-polarization (DP) synthetic aperture radar (SAR) satellite imagery, but there is strong interest in automating this process. Recently launched satellites offer compact polarimetry (CP) imagery that provides more comprehensive polarimetric information compared to DP, which compels the use of CP for automated classification of SAR sea ice imagery. Existing sea ice scene classification algorithms using CP imagery rely on handcrafted features, while neural networks offer the potential of features that are more discriminating. We have developed a new and effective sea ice classification algorithm that leverages the nature of CP data. First, a residual-based convolutional neural network (ResCNN) is implemented to classify each pixel. In parallel, an unsupervised segmentation is performed to generate regions based on CP statistical properties. Regions are assigned a single class label by majority voting using the ResCNN output. For testing, quad-polarimetric (QP) SAR sea ice scenes from the RADARSAT Constellation Mission (RCM) are used, and QP, DP, CP, and reconstructed QP modes are compared for classification accuracy, while also comparing them to other classification approaches. Using CP achieves an overall accuracy of 96.86%, which is comparable to QP (97.16%), and higher than reconstructed QP and DP data by about 2% and 10%, respectively. The implemented algorithm using CP imagery provides an improved option for automated sea ice mapping.

Keywords: RADARSAT Constellation Mission (RCM); synthetic aperture radar (SAR); compact polarimetry; ice types; contextual information; feature learning; segmentation; deep learning

Citation: Taleghanidoozdoozan, S.; Xu, L.; Clausi, D.A. Region-Based Sea Ice Mapping Using Compact Polarimetric Synthetic Aperture Radar Imagery with Learned Features and Contextual Information. *Remote Sens.* **2023**, *15*, 3199. https://doi.org/10.3390/rs15123199

Academic Editor: Yi Luo

Received: 11 May 2023
Revised: 14 June 2023
Accepted: 16 June 2023
Published: 20 June 2023

1. Introduction

Ice maps are essential for applications such as climate change interpretation and ocean navigation [1]. Synthetic aperture radar (SAR) from satellites is the primary source of imagery used to generate sea ice maps. National ice centers, such as the Canadian Ice Service (CIS), rely on trained operators to manually generate sea ice maps primarily using satellite synthetic aperture radar (SAR) imagery, a time-consuming process. Automated sea ice classification methods using SAR imagery have been sought for decades [2].

The RADARSAT Constellation Mission (RCM), the latest generation of Earth observation SAR satellites in Canada, comprises three satellites that operate in different acquisition modes, such as single-polarization, dual-polarization (DP), compact polarimetric (CP), and quad-polarization (QP) [3]. The RCM CP operates in CTLR (right circular transmit and linear receive) mode [4] and generates swaths (500 km) comparable to DP imagery while preserving the phase information between channels, thereby providing more comprehensive scene information than DP [5]. QP swaths are much smaller (20 km) and are not viable for operational ice mapping. Compared to the more extensive literature for sea ice mapping using DP, there exist limited publications that assess CP SAR data for automated sea ice mapping [2,5–12]. Previous sea ice classification methods using CP utilize handcrafted features such as intensity images, polarimetric features, and texture features.

Some classification methods use the reconstructed QP (RQP) data derived from CP SAR to leverage well-known QP parameters whose usage and interpretation are known [2,7]. Existing CP SAR sea ice classification methods, although successful, have limitations.

Using handcrafted features has limitations because these cannot be assured to be a comprehensive representation of all classes and are sensitive to noise and changes in conditions [13]. In addition, feature selection processes are time-consuming and may lead to the loss of important information or strong correlations between features [14]. In contrast, feature learning methods allow a system to automatically extract effective features for specific data and conditions without human intervention [15]. Convolutional neural networks (CNNs) have been used to learn features from SAR imagery in support of ice concentration estimation [16], ice–water classification [17–21], sea ice change detection [22], and ship–iceberg discrimination [23]. Residual-based CNN (ResCNN) methods are able to learn effective feature representations and are highly adaptable to various tasks and datasets [24]. We are not aware of published research that uses deep learning models applied to CP imagery to support sea ice mapping.

The complex Wishart distribution is a known statistical property of the multilook CP coherence matrix, arising from the complex Gaussian distribution of the backscattered field in CP SAR data [25]. Given this knowledge, it would be advantageous to include the Wishart distribution as part of the CP sea ice classification approach to account for the nature of the data. Furthermore, the use of spatial context enhances both the classification accuracy and the algorithmic efficiency [26]. Therefore, the integration of spatial context should be considered in generating sea ice maps.

We propose a new region-based automated sea ice classification methodology that incorporates learned features, spatial context, and statistical properties of various SAR modes. Uniquely, we apply the deep learning algorithm directly to the RCM CTLR CP data—henceforth, we refer to CTLR CP as CP—to generate a pixel-level classification. As a novel contribution, CP is compared to DP, RQP, and QP with regard to generation of accurate sea ice maps. Identifying the most effective mode for SAR sea ice classification supports improved operational algorithmic capability.

A ResCNN model [24] is used to obtain pixel-level sea ice maps by learning sea ice features from CP SAR data. An existing unsupervised semantic segmentation based on statistical characteristics of the CP data [27] is applied to obtain homogeneous and edge-preserved regions. Similar approaches, using appropriate statistical distributions, are implemented for each of the SAR modes under consideration. To generate region-based sea ice maps, as supported by previous studies [2,28], a majority voting process is employed to combine pixel-level classified and segmented images.

Despite the launch of the RCM satellites, there are no RCM CP images available to the public that contain labeled pixels for ice type classification. Consequently, this study relies on RADARSAT-2 QP scenes that have already been labeled by experts from the Canadian Ice Service (CIS) [2] to derive corresponding RCM CP scenes. The region-based sea ice classification approach achieves accurate sea ice maps, demonstrating that CP can achieve comparable sea ice classification performance relative to QP and outperform DP and RQP.

A literature review of the sea ice classification methods using CP SAR data is presented in Section 2. The proposed methodology is explained in Section 3. The experiments and the corresponding results are shown and analyzed in Section 4, and the conclusions are presented in Section 5.

2. Background

In general, classification algorithms utilizing CP can be divided into two categories: algorithms using features derived directly from CP data and algorithms employing reconstructed full QP data derived from CP data. Each of these categories are discussed next.

In the first category, polarimetric features such as $m - \chi$ decomposition features [29] are extracted from the Stokes vector of CP data. Perhaps the first evaluation of CP imagery's ability to differentiate open water from sea ice was visually conducted by

Charbonneau et al. [30]. They used derived CP imagery data from QP aircraft-based SAR images acquired over the Canadian Arctic. Subsequently, several studies then evaluated the capability of CP polarimetric features extracted from the Stokes vector to distinguish different ice types from open water [6,8,9,11,31]. Dabboor et al. [5] derived 23 features for three RCM modes with different resolutions in order to classify first-year ice, multi-year ice, and open water classes. Singha and Ressel [6] proposed a two-step method including feature extraction followed by a supervised classifier to distinguish different ice types. Geldstezer et al. [8] investigated the discrimination capability of 26 CP features in 3 different modes of RCM across 4 different seasons. Additionally, they analyzed the values of the CP features corresponding to each ice type.

In the second category, rather than using CP data directly, the QP covariance matrix is reconstructed from CP data [32,33] and used with QP scene classification methods. Zhang et al. [10] evaluated the ability of CP modes to reconstruct QP information and they recommended using CTLR mode for studying sea ice classification. Ainsworth et al. [34] demonstrated that RQP's potential in classifying crop fields is comparable to that of CP.

In addition to using backscatter measures, handcrafted features can be used to augment the feature set for a sea ice classification task. However, using handcrafted features requires domain expertise, and selecting the proper parameters to generate effective features is time-consuming [35]. Deep learning methods, in contrast, are data-driven and do not require prior knowledge or assumptions, and can automatically learn features from data [35,36], removing the need for manual feature engineering [36]. Thus, it is highly advantageous to evaluate the potential of CP imagery for generating sea ice maps using deep learning techniques.

Combining sea ice maps generated by pixel-level classification with segmented images improves classification accuracy [2,28]. Leigh et al. [28] utilized Iterative Region Growing using Semantics (IRGS) [37] and a global+local (glocal) approach on RADARSAT-2 images to identify homogeneous regions and an SVM classifier to generate pixel-level sea ice maps using gray-level co-occurrence matrix (GLCM) texture and intensity features. The basic IRGS algorithm [37–39] uses intensity images with Gaussian statistics in a spatial context model. CP enhances the measurement potential of radar illumination by providing the 2×2 coherence matrix of the backscattered field which follows the complex Wishart distribution [25,27]. As a result, to fully utilize the information provided by CP data, CP-IRGS [27] should be applied to segment it. Ghanbari et al. [2] employed Polarimetric IRGS (PolarIRGS) [40] to segment RQP images with a support vector machine (SVM) pixel-level classification [41] to label regions using CP polarimetric features.

Taking into account these motivations, we proposed a region-based ResCNN methodology that utilizes learned features, spatial context, and statistical characteristics of CP imagery to classify SAR sea ice scenes. The study also evaluated and compared the potential of CP imagery for generating sea ice maps against comparable approaches for DP, RQP, and QP modes. This comparison is necessary, as different SAR data modes have distinct characteristics that can impact their ability to generate sea ice maps. By considering these differences, the most appropriate data source can be assessed.

The methods proposed by Ghanbari et al. [2] and Leigh et al. [28] were used as baselines against which to compare the performance of the proposed methodology.

3. Methodology

In this section, the proposed methodology is described comprehensively. The proposed region-based classification methodology consists of the following components, as shown in Figure 1:

- The various SAR modes (Section 3.1) each used as source imagery are CP, DP, RQP, and QP as input to the region-based segmentation and pixel-level classification methods;
- A ResCNN model is used to generate the pixel-level sea ice maps by using learned features from each of the modes (Section 3.2);

- Unsupervised segmentation algorithms, which are mode dependent, are used to generate homogeneous, contiguous regions with accurate class boundaries (Section 3.3);
- The segmented and pixel-level classified images are combined by a region-based majority voting approach (Section 3.4).

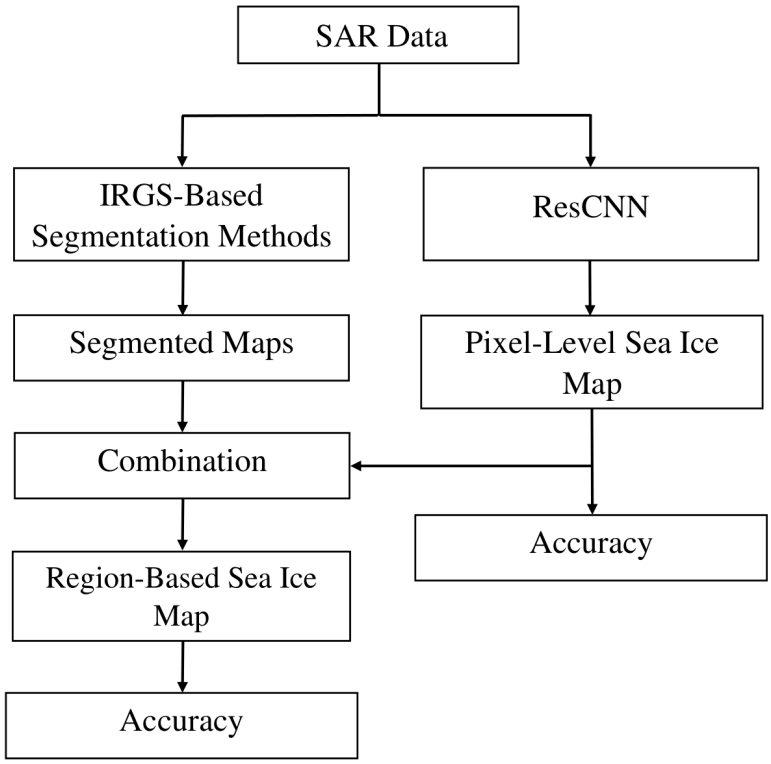

Figure 1. Flowchart of the main steps of the proposed classification method.

To ensure consistency and enable comparisons with the baseline methods, we employed the polarimetric features listed in Table 1 in the same manner as Ghanbari et al. [2]. Smooth FYI, new ice, and open water at low wind speeds are anticipated to result in low RH and RV values. Conversely, rough or ridged FYI, MYI, and open water at high wind speeds are expected to yield higher RH and RV values [42]. The behavior of the conformity coefficient is unknown for sea ice [8]; however, under moderate to high wind speeds, open water is anticipated to have a high conformity coefficient, while wind slicks on open water are expected to exhibit a low conformity coefficient [43,44]. Geldsetzer et al. [8] offered comprehensive insights into the behavior of the CP features for different seasons and incidence angles.

Table 1. List of CP polarimetric and amplitude features.

Name	Description	# a
RH, RV	intensity values of RH and RV channels [45]	2
α	scattering mechanism parameter [46]	1
μ_c	circular polarization ratio [30]	1
u	conformity coefficient [5]	1
ρ	correlation coefficient of RH and RV [5]	1
m	degree of polarization [29]	1
H_i	Shannon entropy, intensity component [5]	1
H_p	Shannon entropy, polarimetric component [5]	1
$m-\chi$	m-chi decomposition of CP data [29]	3
$S_0, \ldots, S_3$	Stokes vector components [47]	4

shows the number of features.

Meanwhile, the same features as Leigh et al. [28] for the RH and RV CP scenes were used. These features are intensity images as well as local average, maximum intensity, and GLCM, including applied second moment, contrast, correlation, dissimilarity, entropy, homogeneity, inverse moment, mean, and standard deviation extracted using three window sizes of 3×3, 9×9, and 17×17. The texture features were then averaged across the four dominant directions, known as isotropic GLCM step directions.

3.1. SAR Data

The mathematical basis of the four SAR modes (QP, CP, RQP, and DP) used in this study are described here.

3.1.1. QP SAR Data

Each pixel in the observed QP imagery is represented by four elements in a 2×2 scattering matrix [48]:

$$\mathbf{S} = \begin{bmatrix} S_{HH} & S_{HV} \\ S_{VH} & S_{VV} \end{bmatrix}, \tag{1}$$

where S_{ij} is complex and ij indicate the transmitted and received polarizations [48], which can be either horizontal (H) or vertical (V). Then, a 3×3 covariance matrix is calculated assuming reciprocity of monostatic radar [48]:

$$\mathbf{C}_{QP} = \begin{bmatrix} \langle |S_{HH}|^2 \rangle & \sqrt{2}\langle S_{HH} S_{HV}^* \rangle & \langle S_{HH} S_{VV}^* \rangle \\ \sqrt{2}\langle S_{HV} S_{HH}^* \rangle & 2\langle |S_{HV}|^2 \rangle & \sqrt{2}\langle S_{HV} S_{VV}^* \rangle \\ \langle S_{VV} S_{HH}^* \rangle & \sqrt{2}\langle S_{VV} S_{HV}^* \rangle & \langle |S_{VV}|^2 \rangle \end{bmatrix}, \tag{2}$$

where $\langle \ldots \rangle$ and * indicate spatial ensemble averaging and the conjugate transpose, respectively. $\mathbf{C}_{QP}$ follows a complex Wishart distribution [48].

3.1.2. Synthesized CP SAR Data

The coherence matrix of CP SAR data is a 2×2 semi-positive definite Hermitian matrix. For a CTLR mode, the coherence matrix is given as follows [7]:

$$\mathbf{C}_{CP} = \begin{bmatrix} \langle | S_{RH}^2 | \rangle & \langle S_{RH} S_{RV}^* \rangle \\ \langle S_{RV} S_{RH}^* \rangle & \langle | S_{RV}^2 | \rangle \end{bmatrix}, \tag{3}$$

where R stands for transmitted right circular polarized wave. $\mathbf{C}_{CP}$ follows a complex Wishart distribution [49]. Based on the observed QP data, CP data can be derived. To derive S_{RH} and S_{RV}, the equations $S_{RH} = (S_{HH} - iS_{HV})/\sqrt{2}$ and $S_{RV} = (S_{HV} - iS_{VV})/\sqrt{2}$ are used [4].

3.1.3. Reconstructed QP SAR Data

Based on the CP data, the QP data can be reconstructed to be used as an alternative representation of the CP data. To reconstruct the 3×3 covariance matrix of QP, reflection symmetry resulting in $\langle S_{HH} S_{HV}^* \rangle = \langle S_{VV}^* S_{HV} \rangle = 0$ and cross-pol ratio must be used [32,50]. Therefore, the reconstructed covariance matrix derived from the CTLR CP mode is expressed as follows [51,52]:

$$\mathbf{C}_{RQP} = \begin{bmatrix} C_{11} - |S_{HV}|^2 & 0 & -iC_{12} + |S_{HV}|^2 \\ 0 & 2\langle |S_{HV}|^2 \rangle & 0 \\ (-iC_{12} + |S_{HV}|^2)^* & 0 & C_{22} - |S_{HV}|^2 \end{bmatrix}, \tag{4}$$

where C_{ij} indicates the elements of C_{CP}. There are several methods to reconstruct QP SAR data using CP data [32,33,53,54]. In this paper, similar to the baseline method [2], an iterative method proposed by Nord et al. [33] was used to calculate $\mathbf{C}_{RQP}$ elements.

3.1.4. DP SAR Data

In contrast to QP and CP, DP data do not include phase information between channels. Therefore, the covariance matrix cannot be calculated. In this study, derived RCM HH and HV intensity channels from QP SAR data were used.

3.2. Sea Ice Classification Using ResCNN Model

Due to the limited availability of annotated SAR data for sea ice classification tasks, overfitting can occur using deep learning models such as ResNet [24] or VGG [55]. A simpler deep learning model was used to alleviate this problem. In this study, a four-block ResCNN model was used and trained by minimizing the multi-class cross-entropy loss function [56]. As indicated in Table 2, each block consisted of two convolution operators, and the number of feature maps in each block was set to 32, 48, 64, and 80. To provide nonlinear expression ability to the ResCNN model, a standard ReLU (rectified linear activation unit) activation function was used [35]. After applying a global average operator on the output of the last block, a fully connected layer was used to map the features into one of K classes.

Table 2. Structure of the CNN model along with the operators.

Layer Name	Output Size	Operators
Block 1	$17 \times 17 \times 32$	$\begin{bmatrix} 3 \times 3 \times 32 \\ 3 \times 3 \times 32 \end{bmatrix}$
Block 2	$9 \times 9 \times 48$	$\begin{bmatrix} 3 \times 3 \times 48 \\ 3 \times 3 \times 48 \end{bmatrix}$
Block 3	$5 \times 5 \times 64$	$\begin{bmatrix} 3 \times 3 \times 64 \\ 3 \times 3 \times 64 \end{bmatrix}$
Block 4	$3 \times 3 \times 80$	$\begin{bmatrix} 3 \times 3 \times 80 \\ 3 \times 3 \times 80 \end{bmatrix}$
Global Average	$1 \times 1 \times 64$	3×3 average pool
Classification	K	$64 \times K$ fully connected
Softmax	K	

To minimize the loss function, the Adam optimizer [57] was employed. The distribution of layers is affected by changing the parameters of previous layers in a CNN model [58]. To overcome this limitation, the batch normalization method was used. To help reduce the risk of overfitting, dropout was applied. After training the ResCNN model, all pixels in the SAR image were classified to obtain pixel-level sea ice maps.

3.3. Obtaining Homogeneous Edge-Preserved Regions

The effective preservation of boundaries between different ice types when generating sea ice maps is achieved through the use of unsupervised region-based segmentation. The resulting regions must meet two criteria: (i) they should be homogeneous, containing only a single class and (ii) they should preserve the boundaries between different classes accurately. The successful IRGS algorithm was chosen because of its effectiveness in segmenting SAR imagery and generating accurate class boundaries [2,28,38,59].

The original IRGS method [37], designed only for SAR amplitude images, was used for the segmentation of sea ice scenes using DP scenes. Yu et al. [40] extended IRGS to PolarIRGS and applied it to a land cover-type dataset. PolarIRGS leverages all available information in QP by designing a feature model based on the complex Wishart distribution and adapting the spatial context model to better capture the specific characteristics of QP. The edge penalty term was measured using the amplitude images of HH, HV, and VV. The PolarIRGS method was performed here to segment sea ice scenes using $\mathbf{C}_{QP}$ and $\mathbf{C}_{RQP}$.

Ghanbari et al. [27] introduced CP-IRGS by similarly modifying IRGS to accommodate CP data. CP scenes were segmented using CP-IRGS, and the RH and RV images were used to measure the required edge-penalty term.

3.4. Combining Pixel-Based Classification and Region-Based Segmentation

The pixel-level sea ice maps generated by ResCNN are generally accurate because ResCNN learns discriminative features during the training process. However, pixel-level sea ice maps have many errors due to the speckle noise causing individual pixels to be assigned to incorrect classes. Combining the pixel-level classified image with edge-preserving regions results in high-precision sea ice maps. To achieve that, a majority voting process was applied to each region to determine the sea ice class labels of regions as follows [2]:

$$l_{r_s} = \max_{j=1}^{K} \sum_{i \in r_s} Vote(l_i)_j, \tag{5}$$

where l_{r_s} indicates the class label of region r_s, K is the total number of ice classes, and $i \in r_s$ represents the pixels that comprise r_s. The term l_i indicates the label of the ith pixel, and $Vote(l_i)_j$ is defined as shown:

$$Vote(l_i)_j = \begin{cases} 1, & \text{if } l_i \text{ belongs to class j} \\ 0, & \text{otherwise} \end{cases} \tag{6}$$

4. Experiments

This section presents the experiments of the ice-type classification and discusses the performance of the classification in two general cases. In case 1, the potential of CP data in generating sea ice maps using the proposed methodology is compared against that of DP, RQP, and QP modes. In case 2, the proposed methodology's performance is compared to that of other baseline methods.

4.1. Study Area and Dataset

In this study, two QP RADARSAT-2 scenes were used to generate the RCM DP and CP SAR data, and the corresponding RQP SAR data were generated as described in Section 3.1. The two QP SAR scenes were acquired in the FQ11 imaging mode with two seconds time difference, identified as Scene 56 and Scene 58 over Barrow Strait, located near Somerset Island in the Canadian Arctic, collected on 5 May 2010. The range $\times$ azimuth resolutions of the scenes were 5.2 $\times$ 7.6 m. The incidence angle range for the scenes was between 30.20° and 32°.

Figure 2a illustrates the location of the two scenes. The study area covered approximately 23 km by 14 km, with five different classes: young ice (YI), first-year ice (FYI), multi-year ice (MYI), new ice (NI), and open water (OW), identified by experts in CIS. Since the backscatter signatures of OW and NI classes are very similar, they were assumed as the same class (OW/NI) [2]. Figure 2b,c show the first element of $\mathbf{C}_{CP}$ of the two derived CP scenes along with the overlaid labeled pixels.

To derive CP SAR data from RADARSAT-2 QP scenes, an RCM simulator developed at the Canada Centre for Mapping and Earth Observation (CCMEO) was used [30]. The scenes were derived for the 30 m RCM medium resolution beam mode with -24 dB noise floor (noise-equivalent sigma zero value). A 9 $\times$ 9 boxcar averaging filter was applied to the SAR data to reduce speckle noise. The RCM HH and HV intensity images were also extracted with the same RCM mode and averaging filter size.

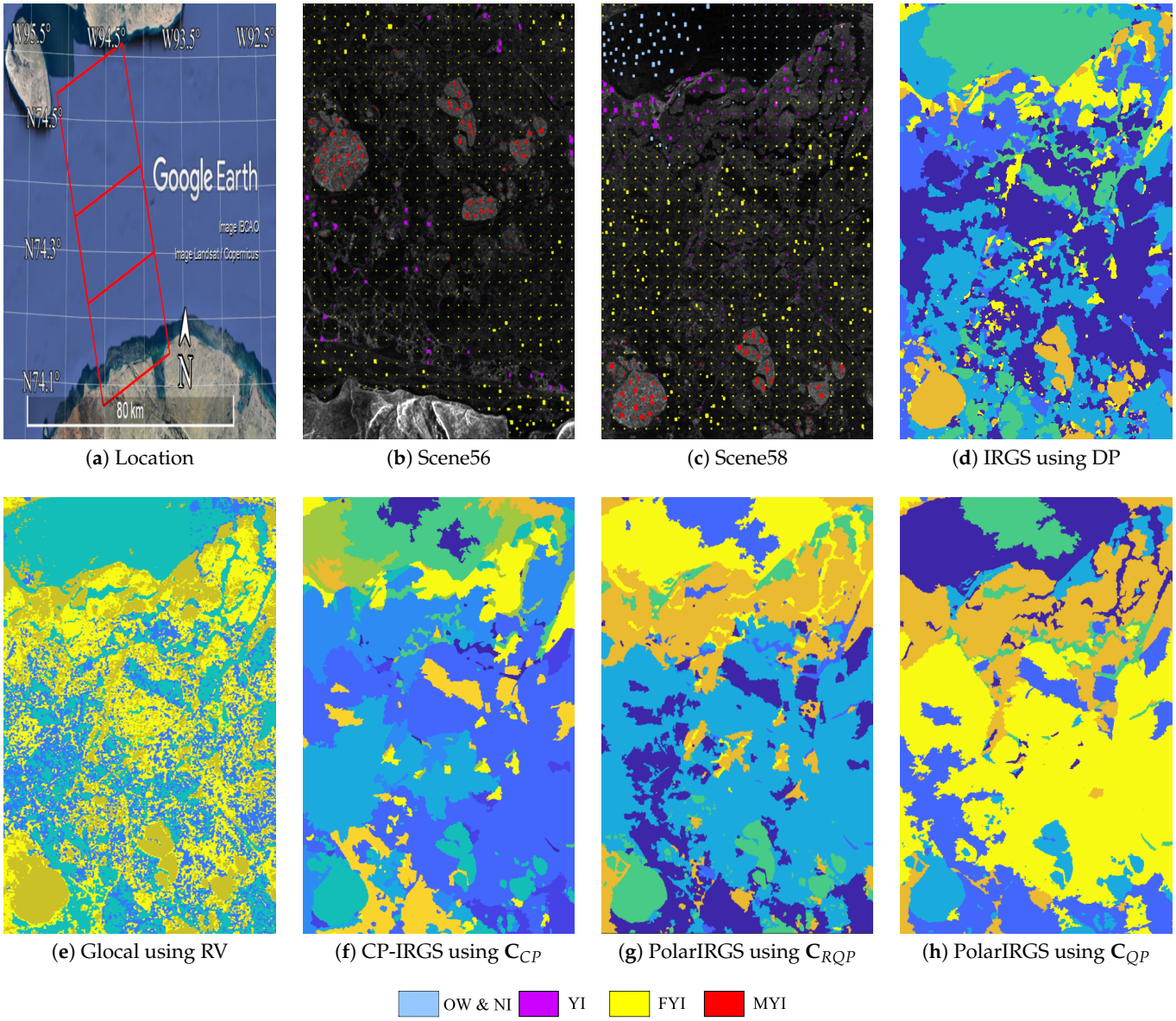

(**a**) Location (**b**) Scene56 (**c**) Scene58 (**d**) IRGS using DP

(**e**) Glocal using RV (**f**) CP-IRGS using $\mathbf{C}_{CP}$ (**g**) PolarIRGS using $\mathbf{C}_{RQP}$ (**h**) PolarIRGS using $\mathbf{C}_{QP}$

Figure 2. (**a**) The locations of the two RADARSAT-2 fine QP scenes in the Barrow Strait. The first element of the covariance matrix of Scenes (**b**) 56 and (**c**) 58, along with the overlaid labeled pixels of open water/new ice class (blue), young ice (violet), first-year ice (yellow), and multi-year ice (red). (**d**–**h**) are the segmentation images obtained using IRGS-based methods.

4.2. Training and Testing Data

The number of labeled pixels specified by CIS experts is approximately 1000. However, due to the large amount of training data required by deep learning methods, we augmented the number of samples by incorporating the CIS's provided samples to guide the collection of additional labeled pixels. CIS experts used the MAGIC software to partition Scene 56 and 58 into a number of grids and assign a label to the central pixel of each grid [60]. Table 3 shows the number of training and test pixels in each class. Scene 56 was used for training, while Scene 58 was used for testing. Since Scene 56 does not include sufficient numbers of OW/NI samples, 2000 OW/NI samples were obtained from Scene 58 to train models. The training samples were used to standardize Scenes 56 and 58. $F \times 17 \times 17$ patches were extracted around each labeled pixel to train the ResCNN models. F stands for the number of input feature maps. In case 1, it corresponded to the absolute values of coherency matrix elements. Thus, F was 2, 3, 4, and 6 for DP, derived CP, RQP, and QP SAR data, respectively. In case 2, F was 16 and 35 for polarimetric and GLCM feature-based baselines, respectively.

The number of training patches in each class was not equal, which is known as an imbalanced dataset problem. To overcome this problem, data augmentation techniques, including horizontal and vertical flips as well as random rotation, were used to expand the number of training patches to 7000 per class.

Table 3. The number of training and testing pixels for each class.

Name	Description	# of Train	# of Test
OW/NI	open water and new ice	2000	3367
YI	young ice	5889	6383
FYI	first-year ice	6395	6383
MYI	multi-year ice	5750	5637

4.3. Model Settings

The learning rate, weight decay, and beta parameters in ADAM optimization [57] were set to 1×10^{-5}, 0.05, 0.9, and 0.999 in the training phase. The batch size and training epochs were 50 and 200, respectively.

SVM is a machine learning algorithm that was used previously in support of sea ice mapping [2,28,59]. The hyperparameters C, Gamma, and Degree for SVM were explored within the ranges $[10^{-2}, 10^{2}]$, utilizing increments of 10 for the kernel functions of linear, polynomial, and radial basis functions. The values of hyperparameters associated with the highest overall classification accuracy (OA) were chosen.

4.4. Comparing CP, DP, RQP, and QP Modes

Figure 3a–d shows pixel-level sea ice maps obtained only by the ResCNN models. The images are resized to fit the page, which may have resulted in some loss of detail. In general, the pixel-level sea ice maps appeared with many erroneous pixels, probably caused by speckle noise. Many YI pixels in the upper part of the scene were erroneously classified as MYI by all models, likely due to the similarity in intensity values between these YI pixels and MYI pixels. The high intensity values observed could be attributed to the presence of dry snowpack on YI [61].

The QP data generated the highest OA of 89.52%, while CP yielded a slightly lower OA of 88.23%, demonstrating that CP data has a comparable ability to provide sea ice maps to QP data. Meanwhile, using RQP achieved an accuracy of 87.24%, which was comparable to CP but also slightly lower than QP. This indicates that RQP did not offer richer information for classification than CP. The lowest OA was obtained by the DP images (80.13%), demonstrating that the polarimetric information in the other three modes are useful in support of accurate classification. As shown in Figure 3a, DP–ResCNN misclassified several OW/NI and YI pixels as FYI.

Figure 3e–h shows the region-level sea ice maps after combining segmentation and classification maps using majority voting. Overall, the region-level results exhibited well-defined homogeneous regions and less noisy classifications when compared to the sea ice maps at the pixel level.

Table 4 presents the performance of ice-type classification on the test sampled data. It shows that the combination of QP–ResCNN and PolarIRGS (QP+PolarIRGS) generated the highest OA (97.16%), which was slightly greater than OA of CP–ResCNN combined with CP–IRGS (CP+CP–IRGS), that achieved an accuracy of 96.86%. This demonstrates that CP data can effectively approximate the QP capability for sea ice mapping. The combination of RQP–ResCNN and PolarIRGS (RQP+PolarIRGS) produced an OA of 94.98%, which was lower than CP+CP–IRGS, which does not motivate its use.

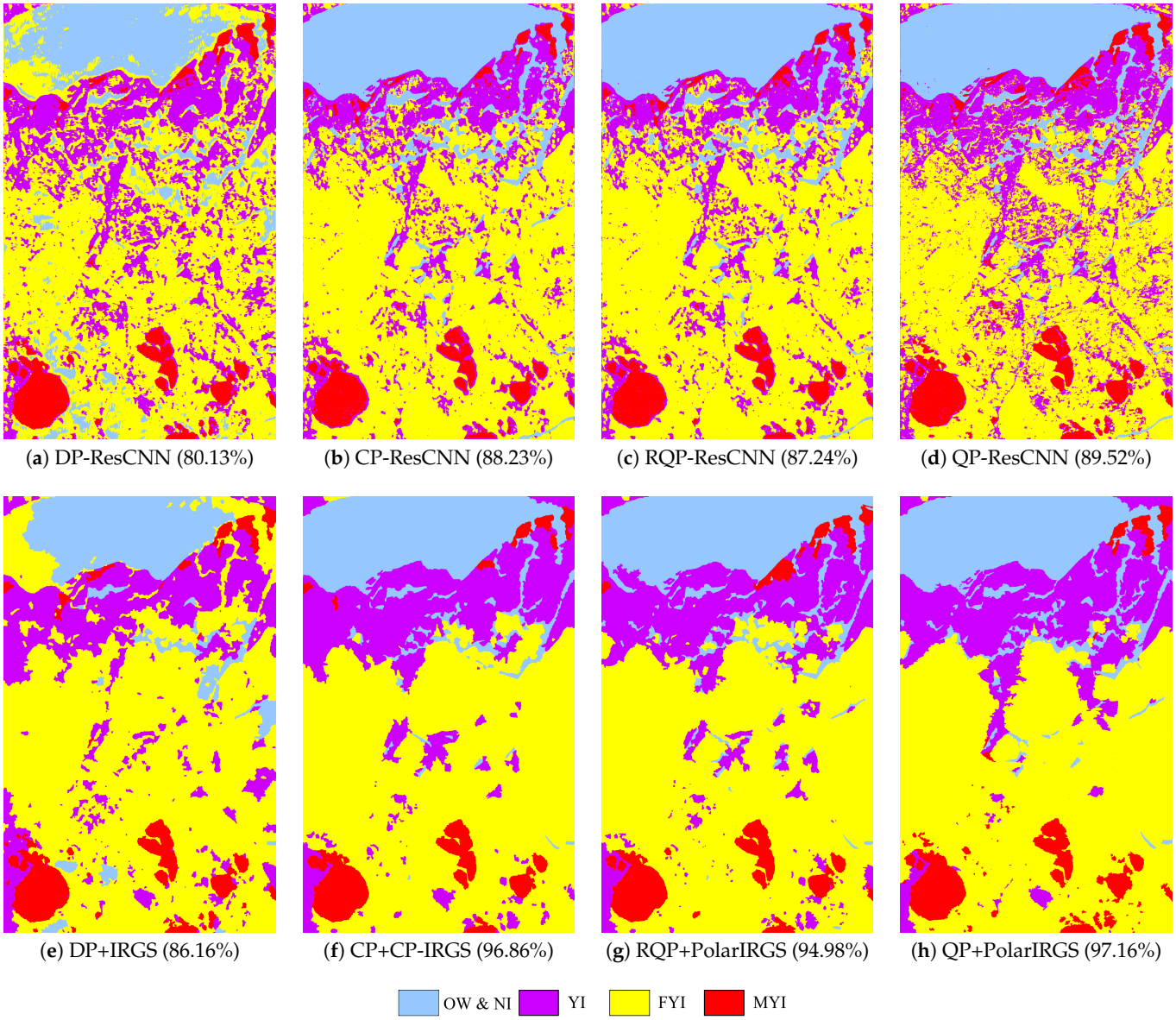

(**a**) DP-ResCNN (80.13%) (**b**) CP-ResCNN (88.23%) (**c**) RQP-ResCNN (87.24%) (**d**) QP-ResCNN (89.52%)

(**e**) DP+IRGS (86.16%) (**f**) CP+CP-IRGS (96.86%) (**g**) RQP+PolarIRGS (94.98%) (**h**) QP+PolarIRGS (97.16%)

Figure 3. (**a**–**d**) Pixel-level sea ice maps generated by the ResCNN feature learning classifier using DP (DP–ResCNN), derived CP (CP–ResCNN), RQP (RQP–ResCNN), and QP SAR data (QP–ResCNN). (**e**–**h**) segmentation combined with ResCNN classification results along with their overall accuracy(OA). It should be noted that the QP results have been rescaled to match CP data size for presentation purposes.

The RQP+PolarIRGS method achieved an MYI user's accuracy of 89.02% by misidentifying 10.86% of the YI test samples as MYI, which mainly included samples in the upper portion of the scene. Both the QP+PolarIRGS and RQP+PolarIRGS methods misclassified several FYI test samples as YI, leading to a decrease of approximately 6% in the YI user's accuracy. In contrast, the CP+CP–IRGS approach could more accurately differentiate between YI and FYI classes.

Table 4. Confusion matrices obtained by the region-based ResCNN models using the amplitude scenes of DP, derived CP, RQP, and QP.

Method		OW/NI	YI	FYI	MYI	User's Accuracy (%)
DP+IRGS	OW/NI	2299	6	234	0	90.55
	YI	1	5053	366	4	93.16
	FYI	1067	164	5778	5	82.38
	MYI	0	1160	5	5628	82.85
	Overall Accuracy (%):					86.16
	Kappa Coefficient:					0.8114
CP+CP-IRGS	OW/NI	3327	32	1	0	99.19
	YI	21	5874	119	5	97.60
	FYI	19	23	6261	7	99.22
	MYI	0	454	2	5625	92.50
	Overall Accuracy (%):					96.86
	Kappa Coefficient:					0.9575
RQP+PolarIRGS	OW/NI	3307	8	4	0	99.064
	YI	41	5655	287	6	94.42
	FYI	19	27	6091	6	99.15
	MYI	0	693	1	5625	89.02
	Overall Accuracy (%):					94.98
	Kappa Coefficient:					0.9320
QP+PolarIRGS	OW/NI	3342	14	4	0	99.46
	YI	23	6155	324	2	94.63
	FYI	2	26	6050	31	99.03
	MYI	0	188	5	5604	96.67
	Overall Accuracy (%):					97.16
	Kappa Coefficient:					0.9614

4.5. Performance Comparison of the Proposed Methodology with the Baselines

Figure 4 shows the sea ice maps generated by the baseline methods by Ghanbari et al. [2] and Leigh et al. [28]. As can be seen in Figure 4a,c, the baseline method by Ghanbari et al. [2] yielded many YI samples misclassified as MYI, whereas the number of misclassified YI samples using the approach by Leigh et al. [28] was lower. This indicates that using GLCM features enables SVM to distinguish MYI samples from YI more effectively than polarimetric features.

The corresponding confusion matrices are displayed in Table 5, which show that the approach proposed by Leigh et al. [28], achieving an OA of 93.90%, performed better than the method suggested by Ghanbari et al. [2], which obtained an OA of 90.52%. In accordance with Figure 4b, the user accuracy of MYI obtained by Ghanbari et al. [2] was 76.94%, which is indicative of the misclassified YI pixels at the upper part of the scene, while the user accuracy of FYI obtained by Leigh et al. [28] was 88.71%, mainly due to the misclassification of YI samples as FYI at the upper part of the scene (Figure 4d).

The approach using ResCNN achieved an 88.23% OA, which was about 1.5% higher than the OA attained by each baseline method. Notably, the ResCNN classifier utilized only amplitude CP scenes, whereas the baseline methods incorporated GLCM and polarimetric features as well. Based on the results presented in Tables 4 and 5, the region-based sea ice classification approach proposed in this study achieved the highest OA of 96.86% compared to the performance of the baseline methods.

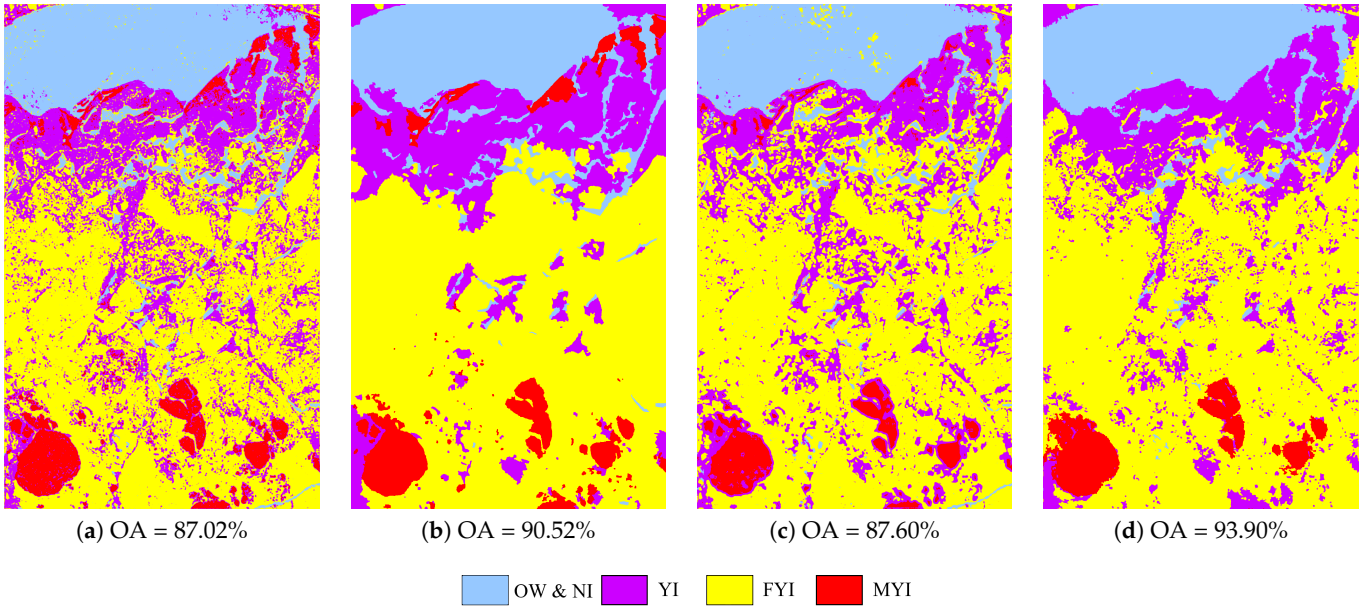

(**a**) OA = 87.02% (**b**) OA = 90.52% (**c**) OA = 87.60% (**d**) OA = 93.90%

Figure 4. Sea ice maps indicating OA for baseline approaches. (**a**) is pixel-based and (**b**) is region-based, using method by Ghanbari et al. [2], while (**c**) is pixel-based and (**d**) is region-based, using method by Leigh et al. [28].

Table 5. Confusion matrices obtained by the region-based baseline methods.

Method		OW/NI	YI	FYI	MYI	User's Accuracy (%)
Ghanbari et al. [2]	OW/NI	3324	7	1	0	99.76
	YI	41	4666	290	3	93.32
	FYI	2	26	6089	5	99.46
	MYI	0	1684	3	5629	76.94
	Overall Accuracy (%):					90.52
	Kappa Coefficient:					0.8719
Leigh et al. [28]	OW/NI	3206	15	4	0	99.41
	YI	2	5791	554	7	91.14
	FYI	159	576	5821	6	88.71
	MYI	0	1	4	5625	99.91
	Overall Accuracy (%):					93.90
	Kappa Coefficient:					0.9171

5. Conclusions

A ResCNN region-based automated sea ice classification algorithm which utilizes CP SAR data is introduced. The proposed approach incorporates learned features with spatial information and leverages the statistical characteristics of the multilook CP coherence matrix to produce accurate sea ice maps. The experimental results revealed that the proposed methodology yields sea ice maps with higher accuracy compared to DP and RQP and performs comparably to QP. These findings suggest that CP data have greater potential than DP for generating sea ice maps, and there is no need to reconstruct QP data from CP. Additionally, the study showed that the potential of CP data in generating sea ice maps is comparable to that of QP.

The ResCNN classifier proposed in this study achieved a higher overall classification accuracy (88.23%) compared to the baseline methods, without the need for polarimetric and GLCM features. These results confirm that feature learning classifiers can improve the accuracy of sea ice maps over traditional machine learning methods such as SVM. By achieving the highest overall accuracy of 96.86%, the proposed region-based sea ice classification methodology outperformed the baseline methods. This highlights the significance

of incorporating the statistical properties of CP data and learned features in the sea ice classification process.

Although the region-based classification methodology is used for generating sea ice maps, it also has potential for addressing other tasks such as land cover classification.

Author Contributions: Conceptualization, S.T., D.A.C. and L.X.; Methodology, S.T., D.A.C. and L.X.; Software, S.T., D.A.C. and L.X.; Validation, S.T.; Formal analysis, S.T.; Investigation, S.T.; Resources, D.A.C. and L.X.; Data curation, S.T.; Writing—original draft preparation, S.T.; Writing—review and editing, D.A.C. and L.X.; Visualization, S.T.; Supervision, D.A.C. and L.X.; Project administration, S.T.; Funding acquisition, D.A.C. and L.X. All authors have read and agreed to the published version of the manuscript.

Funding: This research was funded by the Natural Sciences and Engineering Research Council of Canada (NSERC) under Grant RGPIN-2017-04869, Grant DGDND-2017-00078, Grant RGPAS2017-50794, and Grant RGPIN-2019-06744.

Data Availability Statement: The RADARSAT-2 dataset used in this article is copyright of MacDonald, Dettwiler and Associates Limited (MDA) and not publicly accessible at this time. However, the authors are discussing with MDA to release the dataset for research purposes.

Conflicts of Interest: The authors declare no conflict of interest.

References

1. Barber, D.G. Microwave remote sensing, sea ice and Arctic climate . *Phys. Can* **2005**, *61*, 105–111.
2. Ghanbari, M.; Clausi, D.A.; Xu, L.; Jiang, M. Contextual Classification of Sea-Ice Types Using Compact Polarimetric SAR Data. *IEEE Trans. Geosci. Remote Sens.* **2019**, *57*, 7476–7491. [CrossRef]
3. Charbonneau, F.J.; Arkett, M.; Brisco, B.; Buckley, J.; Chen, H.; Goodenough, D.G.; Liu, C.; McNarin, H.; Poitevin, J.; Shang, J.; et al. Meeting Canadian user needs with the RADARSAT Constellation Mission's compact polarimetry mode: a summary assessment. *Nat. Resour. Can. Ott. Geomat. Can. Open File* **2017**, *34*, 78.
4. Raney, R.K. Hybrid-polarity SAR architecture. *IEEE Trans. Geosci. Remote Sens.* **2007**, *45*, 3397–3404. [CrossRef]
5. Dabboor, M.; Geldsetzer, T. Towards sea ice classification using simulated RADARSAT Constellation Mission compact polarimetric SAR imagery. *Remote Sens. Environ.* **2014**, *140*, 189–195. [CrossRef]
6. Singha, S.; Ressel, R. Arctic sea ice characterization using RISAT-1 compact-pol SAR imagery and feature evaluation: A case study over Northeast Greenland. *IEEE J. Sel. Top. Appl. Earth Obs. Remote Sens.* **2017**, *10*, 3504–3514. [CrossRef]
7. Espeseth, M.M.; Brekke, C.; Anfinsen, S.N. Hybrid-polarity and reconstruction methods for sea ice with L- and C-band SAR. *IEEE Geosci. Remote Sens. Lett.* **2016**, *13*, 467–471. [CrossRef]
8. Geldsetzer, J.; Arkett, M.; Zagon, T.; Charbonneau, F. All-season compact-polarimetry C-band SAR observations of sea ice. *Can. J. Remote Sens.* **2015**, *41*, 485–504. [CrossRef]
9. Li, H.; William, P. Sea ice characterization and classification using hybrid polarimetry SAR. *IEEE J. Sel. Top. Appl. Earth Obs. Remote Sens.* **2016**, *9*, 4998–5010. [CrossRef]
10. Zhang, X.; Zhang, J.; Liu, M.; Meng, J. Assessment of C-band compact polarimetry SAR for sea ice classification. *Acta Oceanol. Sin.* **2016**, *35*, 79–88. [CrossRef]
11. Dabboor, M.; Montpetit, B.; Howell, S. Assessment of the high resolution SAR mode of the RADARSAT Constellation Mission for first year ice and multiyear ice characterization. *Remote Sens.* **2018**, *10*, 594. [CrossRef]
12. Nasonova, S.; Scharien, R.K.; Geldsetzer, T.; Howell, S.; Power, D. Optimal compact polarimetric parameters and texture features for discriminating sea ice types during winter and advanced melt. *Can. J. Remote Sens.* **2018**, *44*, 390–411. [CrossRef]
13. Song, W.; Li, M.; Gao, W.; Huang, D.; Zhenling, M.; Liotta, A.; Perra, C. Automatic sea-ice classification of SAR images based on spatial and temporal features learning. *IEEE Trans. Geosci. Remote Sens.* **2021**, *59*, 9887–9901. [CrossRef]
14. Liu, W.; Wang, W.; Zhao, Q.; Shen, X.; Konan, M. A new feature selection method based on a validity index of feature subset. *IEEE Trans. Geosci. Remote Sens.* **2017**, *92*, 1–8. [CrossRef]
15. Wang, L.; Scott, A.K.; Xu, L.; Clausi, D.A. Sea ice concentration estimation during melt from dual-pol SAR scenes using deep convolutional neural networks: A case study. *IEEE Trans. Geosci. Remote Sens.* **2016**, *54*, 4524–4533. [CrossRef]
16. Lyu, H.; Huang, W.; Mahdianpari, M. Eastern Arctic Sea Ice Sensing: First Results from the RADARSAT Constellation Mission Data. *Remote Sens.* **2022**, *14*, 1165. [CrossRef]
17. Xu, Y.; Scott, A.K. Sea ice and open water classification of SAR imagery using CNN-based transfer learning. In Proceedings of the 2017 IEEE International Geoscience and Remote Sensing Symposium (IGARSS), Fort Worth, TX, USA, 23–28 July 2017; pp. 3262–3265.
18. Ren, Y.; Li, X.; Yang, X.; Xu, H. Development of a Dual-Attention U-Net Model for Sea Ice and Open Water Classification on SAR Images. *IEEE Geosci. Remote Sens. Lett.* **2022**, *19*, 1–5. [CrossRef]

19. Khaleghian, S.; Ullah, H.; Kræmer, T.; Hughes, N.; Eltoft, T.; Marinoni, A. Sea ice classification of SAR imagery based on convolution neural networks. *Remote Sens.* **2021**, *13*, 1734. [CrossRef]
20. Han, Y.; Liu, Y.; Hong, Z.; Zhang, Y.; Yang, S.; Wang, J. Sea ice image classification based on heterogeneous data fusion and deep learning. *Remote Sens.* **2021**, *13*, 592. [CrossRef]
21. Huang, Y.; Ren, Y.; Li, X. Classifying Sea Ice Types from SAR Images Using a U-Net-Based Deep Learning Model. In Proceedings of the 2021 IEEE International Geoscience and Remote Sensing Symposium (IGARSS), Brussels, Belgium, 11–16 July 2021; pp. 3502–3505.
22. Gao, Y.; Gao, F.; Dong, J.; Wang, S. Transferred deep learning for sea ice change detection from synthetic-aperture radar images. *IEEE Geosci. Remote Sens. Lett.* **2019**, *16*, 1655–1659. [CrossRef]
23. Bentes, C.; Frost, A.; Velotto, D.; Tings, B. Ship-iceberg discrimination with convolutional neural networks in high resolution SAR images. In Proceedings of the EUSAR 2016: 11th European Conference on Synthetic Aperture Radar, Hamburg, Germany, 6–9 June 2016; pp. 1–4.
24. He, K.; Zhang, X.; Ren, S.; Sun, J. Deep residual learning for image recognition. In Proceedings of the IEEE Conference on Computer Vision and Pattern Recognition (CVPR), Las Vegas, NV, USA, 27–30 June 2016; pp. 770–778.
25. Guo, S.; Tian, Y.; Li, Y.; Chen, S.; Hong, W. Unsupervised classification based on H/alpha decomposition and Wishart classifier for compact polarimetric SAR. In Proceedings of the 2015 IEEE International Geoscience and Remote Sensing Symposium (IGARSS), Milan, Italy, 26–31 July 2015; pp. 1614–1617.
26. Khedama, R.; Belhadj-Aissaa, A. Contextual classification of remotely sensed data using MAP approach and MRF. *ISPRS J. Photogramm. Remote Sens.* **2004**, *35*, 11–16.
27. Ghanbari, M.; Clausi, D.A.; Xu, L. CP-IRGS: A Region-Based Segmentation of Multilook Complex Compact Polarimetric SAR Data. *IEEE J. Sel. Top. Appl. Earth Obs. Remote Sens.* **2021**, *14*, 6559–6571. [CrossRef]
28. Leigh, S.;Wang, Z.; Clausi, D.A. Automated ice–water classification using dual polarization SAR satellite imagery. *IEEE Trans. Geosci. Remote Sens.* **2013**, *52*, 5529–5539. [CrossRef]
29. Raney, R.K.; Cahill, J.; Patterson, G.W.; Bussey, D.J. The m-chi decomposition of hybrid dual-polarimetric radar data with application to lunar craters. *J. Geophys. Res. Planets* **2012**, *117*. [CrossRef]
30. Charbonneau, F.J.; Brisco, B.; Raney, R.K.; McNairn, H.; Liu, C.; Vachon, P.W.; Shang, J.; DeAbreu, R.; Champagne, C.; Geldsetzer, A.M.; et al. Compact polarimetry overview and applications assessment. *Can. J. Remote Sens.* **2010**, *36*, S298–S315. [CrossRef]
31. Espeseth, M.M.; Brekke, C.; Johansson, A.M. Assessment of RISAT-1 and RADARSAT-2 for sea ice observations from a hybrid-polarity perspective. *Remote Sens.* **2017**, *9*, 1088. [CrossRef]
32. Souyris, J.-C.; Imbo, P.; Fjortoft, R.; Mingot, S.; Lee, J.S. Compact polarimetry based on symmetry properties of geophysical media: The $\pi/4$ mode. *IEEE Trans. Geosci. Remote Sens.* **2005**, *43*, 634–646. [CrossRef]
33. Nord, M.E.; Ainsworth, T.L.; Lee, J.; Stacy, N.J. Comparison of compact polarimetric synthetic aperture radar modes. *IEEE Trans. Geosci. Remote Sens.* **2008**, *47*, 174–188. [CrossRef]
34. Ainsworth, T.L.; Kelly, J.P.; Lee, J.-S. Classification comparisons between dual-pol, compact polarimetric and quad-pol SAR imagery. *ISPRS J. Photogramm. Remote Sens.* **2009**, *64*, 464–471. [CrossRef]
35. Goodfellow, I.; Bengio, Y.; Courville, A. *Deep Learning*; MIT Press: Cambridge, MA, USA, 2016; pp. 203–218, 277–282. ISBN 9780262337434.
36. Bengio, Y.; Courville, A.; Vincent, P. Representation learning: A review and new perspectives. *IEEE Trans. Pattern Anal. Mach. Intell.* **2013**, *35*, 1798–1828. [CrossRef]
37. Yu, Q.; Clausi, D.A. IRGS: Image segmentation using edge penalties and region growing. *IEEE Trans. Pattern Anal. Mach. Intell.* **2008**, *30*, 2126–2139.
38. Yu, Q.; Clausi, D.A. SAR sea-ice image analysis based on iterative region growing using semantics. *IEEE Trans. Geosci. Remote Sens.* **2007**, *45*, 174–188. [CrossRef]
39. Qin, A.K.; Clausi, D.A. Multivariate image segmentation using semantic region growing with adaptive edge penalty. *IEEE Trans. Image Process.* **2010**, *19*, 2157–2170. [CrossRef] [PubMed]
40. Yu, P.; Qin, A.K.; Clausi, D.A. Unsupervised polarimetric SAR image segmentation and classification using region growing with edge penalty. *IEEE Trans. Geosci. Remote Sens.* **2011**, *50*, 1302–1317. [CrossRef]
41. Cortes, C.; Vapnik, V. Support-vector networks Machine. *Mach. Learn.* **1995**, *20*, 237–297. [CrossRef]
42. Geldsetzer, T.; Charbonneau, F.; Arkett, M.; Zagon, T. Ocean wind study using simulated RCM compact-polarimetry SAR. *Can. J. Remote Sens.* **2015**, *41*, 418–430. [CrossRef]
43. Zhang, B.; Perrie, W.; Li, X.; Pichel, W.G. Mapping sea surface oil slicks using RADARSAT-2 quad-polarization SAR image. *Geophys. Res. Lett.* **2011**, *38*. [CrossRef]
44. Geldsetzer, T.; Van Der Sanden, J.J. Identification of polarimetric and nonpolarimetric C-band SAR parameters for application in the monitoring of lake ice freeze-up. *Can. J. Remote Sens.* **2013**, *39*, 263–275. [CrossRef]
45. Dubois-Fernandez, P.C.; Souyris, J.C.; Angelliaume, S.; Garestier, F. The compact polarimetry alternative for spaceborne SAR at low frequency. *IEEE Trans. Geosci. Remote Sens.* **2008**, *43*, 3208–3222. [CrossRef]
46. Cloude, S.R.; Goodenough, D.G.; Chen, H. Compact decomposition theory for L-Band satellite radar applications. *IEEE Trans. Geosci. Remote Sens. Symp.* **2012**, *43*, 5097–5100.
47. Raney, R.K. Dual-polarized SAR and stokes parameters. *IEEE Geosci. Remote Sens. Lett.* **2006**, *3*, 317–319. [CrossRef]

48. Lee, J.-S.; Pottier, E. *Polarimetric Radar Imaging: From Basics to Applications*, 1st ed.; CRC Press: Boca Raton, FL, USA, 2009; ISBN 9781420054989.
49. Goodman, N.R. Statistical analysis based on a certain multivariate complex Gaussian distribution (an introduction). *Ann. Math. Stat.* **1963**, *34*, 152–177. [CrossRef]
50. Chang, Y.; Zhao, L.; Shi, L.; Nie, Y.; Hui, Z.; Xiong, Q.; Li, P. Polarimetric calibration of SAR images using reflection symmetric targets with low helix scattering. *Int. J. Appl. Earth Obs. Geoinf.* **2021**, *104*, 102559. [CrossRef]
51. Nghiem, S.V.; Yueh, S.H.; Kwok, R.; Li, F.K. Symmetry properties in polarimetric remote sensing. *Radio Sci.* **1992**, *27*, 693–711. [CrossRef]
52. Denbina, M.; Collins, M.J. Iceberg detection using compact polarimetric synthetic aperture radar. *Atmos. Ocean* **2012**, *50*, 437–446. [CrossRef]
53. Yin, J.; Moon, W.; Yang, J. Model-based pseudo-quad-pol reconstruction from compact polarimetry and its application to oil-spill observation. *J. Sens.* **2015**, *2015*, 734848. [CrossRef]
54. Collins, M.J.; Denbina, M.; Atteia, G. On the reconstruction of quad-pol SAR data from compact polarimetry data for ocean target detection. *IEEE Trans. Geosci. Remote Sens.* **2012**, *51*, 591–600. [CrossRef]
55. Simonyan, K.; Zisserman, A. Very deep convolutional networks for large-scale image recognition. *arXiv* **2014**, arXiv:1409.1556.
56. Murphy, K.P. *Machine Learning: A Probabilistic Perspective*; MIT Press: Cambridge, MA, USA, 2012; p. 57. ISBN 9780262018029.
57. Kingma, D.P.; Ba, J. Adam: A method for stochastic optimization. *arXiv* **2014**, arXiv:1412.6980.
58. Ioffe, S.; Szegedy, C. Batch normalization: Accelerating deep network training by reducing internal covariate shift. *arXiv* **2015**, arXiv:1502.03167.
59. Hoekstra, M.; Jiang, M.; Clausi, D.A.; Duguay, C. Lake ice-water classification of RADARSAT-2 images by integrating IRGS Segmentation with pixel-based random forest labeling. *Remote Sens.* **2020**, *12*, 1425. [CrossRef]
60. Clausi, D.A.; Qin, A.K.; Chowdhury, M.S.; Yu, P.; Maillard, P. MAGIC: MAp-guided ice classification system. *Can. J. Remote Sens.* **2010**, *36*, S13–S25. [CrossRef]
61. Tsai, Y.S.; Dietz, A.; Oppelt, N.; Kuenzer, C. Remote sensing of snow cover using spaceborne SAR: A review. *Can. J. Remote Sens.* **2019**, *11*, 1456. [CrossRef]